



HAL
open science

An Ultra-Thin Near-Perfect Absorber via Block Copolymer Engineered Metasurfaces

Cian Cummins, Quentin Flamant, Ranjeet Dwivedi, Alberto Alvarez-Fernandez, Nils Demazy, Ahmed Bentaleb, Gwenaelle Pound-Lana, Marc Zelsmann, Philippe Barois, Georges Hadziioannou, et al.

► **To cite this version:**

Cian Cummins, Quentin Flamant, Ranjeet Dwivedi, Alberto Alvarez-Fernandez, Nils Demazy, et al.. An Ultra-Thin Near-Perfect Absorber via Block Copolymer Engineered Metasurfaces. *Journal of Colloid and Interface Science*, 2022, 609, pp.375-383. 10.1016/j.jcis.2021.11.163 . hal-03547419

HAL Id: hal-03547419

<https://hal.science/hal-03547419>

Submitted on 28 Jan 2022

HAL is a multi-disciplinary open access archive for the deposit and dissemination of scientific research documents, whether they are published or not. The documents may come from teaching and research institutions in France or abroad, or from public or private research centers.

L'archive ouverte pluridisciplinaire **HAL**, est destinée au dépôt et à la diffusion de documents scientifiques de niveau recherche, publiés ou non, émanant des établissements d'enseignement et de recherche français ou étrangers, des laboratoires publics ou privés.

An Ultra-Thin Near-Perfect Absorber via Block Copolymer Engineered Metasurfaces

Cian Cummins,^{†,‡,*} Quentin Flamant,[†] Ranjeet Dwivedi,[†] Alberto Alvarez-Fernandez,[§] Nils Demazy,[‡] Ahmed Bentaleb,[†] Gwenaelle Pound-Lana,[°] Marc Zelsmann,[°] Philippe Barois,[†] Georges Hadziioannou,[‡] Alexandre Baron,[†] Guillaume Fleury,^{‡,*} Virginie Ponsinet^{†*}

[†] Univ. Bordeaux, CNRS UMR 5031, Centre de Recherche Paul Pascal, 115 Avenue Schweitzer, 33600 Pessac, France.

[‡] Univ. Bordeaux, CNRS, Bordeaux INP, LCPO, UMR 5629, F-33600, Pessac, France.

[§]Department of Chemical Engineering, University College London, Torrington Place, London WC1E 7JE, U.K.

[°]University of Grenoble Alpes, CNRS, CEA/LETI Minatec, Grenoble INP, LTM, 38000 Grenoble, France

Abstract

Producing ultrathin light absorber layers is attractive towards the integration of lightweight planar components in electronic, photonic, and sensor devices. In this work, we report the experimental demonstration of a thin gold (Au) metallic metasurface with near-perfect visible absorption ($\sim 95\%$). Au nanoresonators possessing heights from 5 - 15 nm with sub-50 nm diameters were engineered by block copolymer (BCP) templating. The Au nanoresonators were fabricated on an alumina (Al_2O_3) spacer layer and a reflecting Au mirror, in a film-coupled nanoparticle design. The BCP nanopatterning strategy to produce desired heights of Au nanoresonators was tailored to achieve near-perfect absorption at ≈ 600 nm. The experimental insight described in this work is a step forward towards realizing large area flat optics applications derived from subwavelength-thin metasurfaces.

Keywords: Block copolymers, metasurfaces, perfect absorbers, nanoresonators, flat optics.

1. Introduction

Absorbers have an important role to play in optoelectronic devices and can be tuned across the electromagnetic spectrum for use in thermal emitters,[1] optical sensors,[2] photovoltaics,[3] optical modulators,[4] or photochemistry.[5] A significant breakthrough in recent years relates to the use of metasurface (MS) perfect absorbers,[6],[7],[8],[9],[10],[11],[12] in which light can be absorbed in very thin layers of matter (thinner than visible wavelengths) for use in optical-based devices. MSs are an attractive platform for fabricating next-generation photonic components, including perfect absorbers, and exhibit unique optical properties induced by abrupt changes imparted to the incident light by a slab of matter of subwavelength thickness. The modification in the wavefront of light is derived from the subwavelength nature of the metallic (or dielectric) MS features, often referred to as optical nanoscatterers or nanoresonators.[13][14] The subwavelength scale of MS nanoresonators eliminates reliance on the propagation effect of refractive materials that are used in traditional optical components and transformation optics.[15] In contrast, the isolated nanoresonator size, shape, and orientation in MSs can be engineered to allow alteration of incident light to precisely manipulate phase and amplitude profiles.

Reports on dense (*i.e.* sub-100 nm period) MS absorber features are scarce, since simple one-layer assemblies of electric dipolar nanoresonators cannot be designed to absorb more than 50% of the incident energy. However, total absorption can be reached if the nano-objects show a relatively large size or a complex structuration to present strong multipolar or magnetic resonances in addition to simple dipolar electric

responses.[16][17] On the other hand, bilayer structuration for MS-based perfect absorption can be designed on an adapted Babinet principle[18] or with the use of a back reflector in order to suppress transmission. Among the latter, two types of designs have been studied. The first design relies on the coupling between a nanoresonator layer and a metallic mirror obtained with a thin controlled spacer layer, also called gap plasmon resonator MSs.^[19] The lateral resonator size and dielectric spacer thickness in this design are crucial. And the absorption effect is related to the electromagnetic field being highly concentrated in the dielectric gap due to constructively interfering gap plasmons reflected at the resonator edges. Fabrication steps must therefore allow for a precise nanostructure control, which poses a technological challenge in terms of large-scale production. The second type of design with a back reflector is based on a Fabry-Perot cell, with a distance between the mirror and the resonators commensurate with the working wavelength, also referred to as Salisbury screens.[20][21] There are wide reports on MS-based absorbers produced using expensive and low-throughput fabrication processes (*e.g.* electron beam, ion beam or extreme UV lithography, etc.) Low cost self-assembly fabrication methodologies, and in particular use of nanocolloidal resonators,[22] have shown promise in the metamaterials field. Several mechanisms have been experimentally demonstrated for the property of MS-based perfect light absorption. For example, Akselrod *et al.* showed the efficacy of wet-chemistry synthesised 75 nm diameter Ag nanocubes on a polymer spacer layer as a near-perfect absorber for visible to near infra-red absorption.[23] Large area near-perfect absorption (92%) was shown with 50 nm-diameter Au nanoparticles randomly distributed on top of a 35 nm Ge₂Sb₂Te₅ layer.[24] Similar results were shown with core-shell Au@SiO₂ resonators randomly arranged onto an aluminium nanofilm.[25]

Simple colloid deposition techniques, however, may lack reproducibility and precise control over the local positional order of 2D nanoresonators. Moreover, a technique that is complementary to traditional top-down photolithography would be attractive. In this regard, one feasible option with the capacity to surmount this critical MS bottleneck is based upon block copolymer (BCP) self-assembly.[26] Thin film BCP templates allow patterning over wafer-scale areas with feature diameters typically ranging from 5-50 nm and periods below 100 nm.[27].[28],[29],[30] These fundamental pattern parameters are dictated by the constituent BCP material where two polymers are covalently bonded in a di-BCP system. Precise synthesis to tune BCP volume fraction (f) can result in morphologies of spheres, cylinders, gyroids, or lamellae from a di-BCP, while the overall molecular weight (M_n) of the BCP leads to morphological pitch control. BCP-based fabrication methodologies have been successfully applied to achieve different bulk metamaterials or nanophotonics properties.[31],[32],[33],[34] The BCP template can be utilized as a sacrificial scaffold to write dense metal and dielectric material patterns, and MSs derived from BCPs have been explored.[35] For instance, Hulkkonen *et al.* fabricated an all Au broadband absorber using a template stripping technique after defining dense patterns in a silicon substrate from pattern transfer of poly(styrene-*b*-2-vinylpyridine) (PS-*b*-P2VP).[36] The resulting Au nanodomes with heights of 60 nm absorbed 97% of incident light in the visible range 320–650 nm, due to the plasmon gap effect in the Au structure. An early example from Bent and co-workers described the use of a metamaterial absorber array coated using atomic layer deposition (ALD) to form an absorbing nanocomposite.[37] Isolated Au dots templated by PS-*b*-PMMA performed best with SnS_x or ZnO ALD coating. The Au nanocomposites were fabricated on a silicon dioxide spacer layer on an ion beam deposited Al reflector plane producing visible light absorption up to 99 %. BCPs were also used to demonstrate an enhanced and tunable

refractive index of Au MSs to 3.2 and 5 respectively through selective Au salt impregnation with PS-*b*-P2VP[38] and via a lift-off process using PS-*b*-PMMA BCP.[39] We describe a system that exhibits near-perfect absorption based on film-coupled nanoparticle assemblies which harnesses the use of vacuum deposition tools and a scalable patterning strategy. BCP templates enabled the fabrication of Au MSs with a feature size of *ca.* 40 nm and a pitch of *ca.* 68 nm. Our approach opens up a flexible methodology to precisely tune nanostructure height, *e.g.* 5-15 nm and resulting wavelength absorption range. The inherent ability to tailor MS features with precision is extremely appealing and surpasses various other wet chemical approaches that cannot be processed in thin-film form. We present key experimental parameters guided by numerical simulations to show the effect of Au MS height and Al₂O₃ spacer layer thickness on absorption properties.

2. Experimental

2.1. Simulations. The MS optical response of the film-coupled nanoparticle design was modelled using the finite-element method (FEM) implemented in the commercial software COMSOL Multiphysics[®].

2.2 Materials. Poly(styrene)-*stat*-poly(methyl methacrylate) (PS-*stat*-PMMA) copolymer ($M_n = 13.6 \text{ kg/mol}$; $D = 1.23$; $f_{PS} = 0.63$) was provided by ARKEMA and was synthesized by nitroxide-mediated radical polymerization using BlocBuilder[®] MA-HEA-SG1 alkoxyamine.[40] A cylinder forming PS-*block*-PMMA (PS-*b*-PMMA, $M_{nPS} = 140 \text{ kg mol}^{-1}$; $M_{nPMMA} = 65 \text{ kg mol}^{-1}$, denoted as PSPMMA205) and a lamellar forming PS-*b*-PMMA ($M_{nPS} = 5 \text{ kg mol}^{-1}$; $M_{nPMMA} = 5 \text{ kg mol}^{-1}$ denoted as PSPMMA10) were purchased from Polymer Source, Inc., Canada and were used without further purification.

A PS-*b*-PMMA BCP blend (4 : 1, PSPMMA205 : PSPMMA 10) solution consisting of toluene solutions of 1.75 wt % PSPMMA205 and 1 wt. % PSPMMA10 were used to form well-ordered hexagonally packed cylinders. Propylene glycol methyl ether acetate (PGMEA) (Reagent Plus, 99.5%), toluene (Reagent Plus, 99.5%), and tetrachloroauric acid (HAuCl₄) (99.999% trace metals basis) were purchased from Merck.

2.3. Wafer Fabrication. Blanket silicon (Si) wafers with a native oxide layer (= 2 nm) were purchased from Si-Mat Silicon Materials. Blanket Si substrates were used initially to define the optimum self-assembly conditions of PS-*b*-PMMA. The following details the processes required to create the metal-insulator-metal (MIM) substrate. Firstly, a 10 nm chromium (Cr) adhesion layer was deposited by thermal evaporation (rate = 0.10 nm/sec). Thereafter, a uniform Au reflector layer of 100 nm was thermally deposited (rate = 0.20 nm/sec). The alumina (Al₂O₃) spacer layer was deposited by atomic layer deposition (ALD) using an Ultratech SAVANNAH G2 tool. The exposure and purge times used in this study were 60 s and 300 s, respectively, resulting in Al₂O₃ spacer thicknesses of = 9 – 42 nm as measured by ellipsometry (see SI Figure S1).

2.4. PS-*b*-PMMA Block Copolymer Template Formation. To promote vertical orientation of the PMMA cylinders, 2 wt. % PS-*stat*-PMMA in PGMEA was deposited at 2000 rpm for 30 secs (ramp, 5 secs) on SiO₂ wafers or Al₂O₃ coated Au mirrors, and baked at 230°C on a hotplate in air for 5 minutes. After baking, the PS-*stat*-PMMA modified wafers were rinsed thoroughly in PGMEA to remove excess material leading to 7 nm thick grafted layer. Thereafter, the PS-*b*-PMMA blend solution was deposited at 2000 rpm forming ≈ 75 nm thick films. PS-*b*-PMMA BCP samples were baked at 230°C on a hotplate in a nitrogen atmosphere for 1.5 hrs to avoid thermal degradation. Annealing produced vertical PMMA cylinder formation (see SI Figure S2), and the PS-*b*-PMMA

BCP films were then exposed to UV light (254 nm) for 1 h to promote PMMA chain scission. Next, the UV-treated PS-*b*-PMMA BCP films were immersed in an acetic acid solution for 30 min to remove PMMA material. Films were then rinsed with ethanol and dried with N₂. To ensure complete opening of the pore channel to the substrate as well as enlargement of the pore diameters, a two-step plasma etch was performed consisting of: Step I - O₂/Ar plasma etch with a flow rate of 5 sccm/45 sccm, power of 30 W for 10 sec and Step II - O₂ plasma etch with a flow rate of 30 sccm, power of 30 W for a duration of 15 sec to produce a porous PS template.

2.5. Au Nanoresonator MS Formation. Au MS features were formed via thermal evaporation onto the porous PS template with thicknesses of 5 nm - 15 nm. After thermal evaporation, PS template lift-off was achieved by sonication in toluene (at 70°C) for up to 60 mins to produce Au nanoresonators atop the Al₂O₃ spacer layer.

2.6. Structure Characterization. Block Copolymer Features, Au Nanoresonator MSs.

Atomic force microscopy (AFM, Dimension Fast Scan, Bruker) was used in tapping mode to characterize the surface morphology of PS-*b*-PMMA BCP films. Silicon cantilevers (Fastscan-A) with a nominal tip radius of 5 nm, a spring constant of about 18 N m⁻¹, and a resonance frequency of about 1400 kHz were used. Scanning electron microscopy (SEM) images were obtained using a JEOL 7800-E Prime SEM in super high resolution gentle beam (GBSH) mode with an accelerating voltage of 1 kV. Scanning transmission electron microscopy was carried out using a Helios 450S tool. The cross-section area (30 micron x 2 micron) to be milled was first capped with protective layers deposited as follows: a 100 nm layer of electron beam deposited carbon to enhance contrast during imaging versus the metal features, a 200 nm thick layer of electron beam

deposited platinum (5kV, 26 nA), and then followed by 500 nm thick layer of ion beam deposited platinum (30kV, 0.43 nA). The area of interest was milled under focused ion beam (FIB), transferred to a grid, and thinned under FIB to a thickness of approx. 300 nm for STEM imaging (29 kV, 50 pA). Grazing incidence small angle X-ray scattering (GISAXS) experiments were performed at the Centre de Recherche Paul Pascal (CRPP) at Université de Bordeaux using a high resolution X-ray spectrometer Xeuss 2.0 from Xenoxs operating with a radiation wavelength of $\lambda = 0.154$ nm. 2D scattering patterns were collected using a PILATUS 300K Dectris detector with a sample-to-detector distance of 2350 mm. The beam center position and the sample to detector distance were calibrated using a silver behenate standard sample. GISAXS patterns were reduced using the GIXSGUI package,[41] where $q_y = 2\pi/\lambda[\sin(2\theta_f) \cos(\alpha_f)]$ and $q_z = 2\pi/\lambda[\sin(\alpha_f) + \sin(\alpha_i)]$ are the modulus of the scattering vectors components in the direction parallel and perpendicular to the substrate plane and α_i , $2\theta_f$ and α_f are the incident and scattering angles in the horizontal and vertical directions, respectively. X-ray reflectivity (XRR) measurements were carried out in a θ - 2θ configuration at CRPP at Université de Bordeaux. X-rays were produced by a Rigaku MM007_HF rotating copper-anode generator ($\lambda = 0.154$ nm) which is equipped with a multilayer collimating monochromator from Osmic. Samples of interest were mounted on a three-circle Huber goniometer and the reflected signal was collected with a Peltier-cooled solid-state detector XR-100CR from Amptek Inc (residual noise = 10^{-2} cts/s). The beam at sample position was $0.2 \times 2 \text{ mm}^2$ and the resolution along the normal to the substrate was $\Delta q_z = 0.018 \text{ nm}^{-1}$ FWHM. Recorded data were fitted to a scattering length density profile using GenX 2.4.10 software.[42]

2.7. Optical Study. A UV–visible-NIR Microspectrophotometer model 20/20 PV from CRAIC Technologies was used to measure the absorption spectra of fabricated Au metasurfaces. Reflectance spectra were acquired on $50\ \mu\text{m} \times 50\ \mu\text{m}$ areas using a 10x objective with a small numerical aperture (0.2) to provide near-normal incidence measurements. To compute the absolute reflectance of the samples, a reference scan was recorded on a gold mirror. At least three areas on each sample were recorded to ensure accuracy. Since transmission is zero in our samples, absorption was obtained by simple subtraction of the reflectance, considering $R+A=1$.

3. Results and Discussion

3.1. Simulations

The film-coupled nanoparticle design simulated here is represented schematically in Figure 1 (a), consisting of Au nanoresonators of circular footprint with diameter $D = 42$ nm and height H_{Au} on a triangular lattice with center-to-center distance $d_{cc} = 68$ nm. The Au nanoresonators are fabricated on an Al_2O_3 layer of thickness H_{sp} and a 100 nm thick Au reflector layer. A Cr layer of thickness 10 nm, used for adhesion, is also considered between the reflector layer and the Si substrate. Firstly, we optimized the values of H_{sp} and H_{Au} for maximum absorption. In our calculations, the structure is considered to be illuminated by a plane wave incident normally from the top. The refractive index data of Si, Cr, Au and Al_2O_3 layers are taken from reference [43]. Examples of the simulated absorption spectra are shown in Figure 1 (b), showing perfect absorption for a specific set of parameters e.g. $H_{Au} = 15$ nm and $H_{sp}=22$ nm. At the perfect absorption wavelength, incident light is perfectly coupled to the highly localized gap plasmon mode supported by nanoresonator, spacer and bottom reflector layer. This can be visualized from Fig. 1(c), showing the norm of electric and magnetic fields distributions in the x-z plane passing

through the centre of the unit cell, which are normalized, respectively, with the incident electric and magnetic field amplitudes. Figure 1(d) and 1(e), respectively, shows the variation of the maximum absorption wavelength and value when the spacer thickness H_{sp} is varied in the range $3 \text{ nm} \leq H_{sp} \leq 45 \text{ nm}$, for different values of H_{Au} between 5 and 30 nm. It may be noted that in the considered range of H_{Au} , perfect absorption can be achieved at a specific value of H_{sp} , which is $\sim 27 \text{ nm}$ for $H_{Au} = 5 \text{ nm}$ and $H_{sp} \sim 22 \text{ nm}$ for $H_{Au} \geq 10 \text{ nm}$. Furthermore, for $H_{Au} \geq 15 \text{ nm}$ the resonance wavelength and the absorbance have negligible variation with H_{Au} . Consequently, we targeted the fabrication of Au nanoresonators with H_{Au} varying between 5-15 nm.

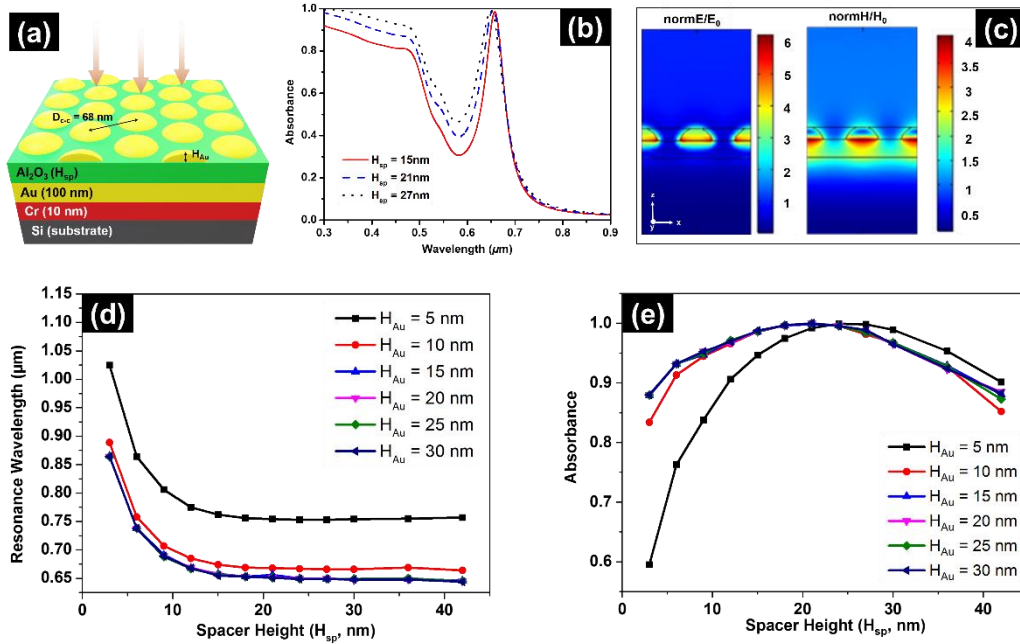


Figure 1. (a) Schematic of the considered gap plasmon absorber system. (b) Simulated absorption spectra at $H_{Au} = 15 \text{ nm}$ and $H_{sp} = 16, 21$ and 27 nm . (c) At perfect absorption ($\lambda = 0.65 \mu\text{m}$), simulated maps in the x - z plane passing through the centre of the unit cell, of the electric and magnetic fields, normalized, respectively, with the incident electric and magnetic field amplitudes. Variation of the resonance wavelength (d), and maximum absorption value (e) with Al_2O_3 spacer thickness (H_{sp}), and for Au height (H_{Au}) varying between 5 and 30 nm. Note the H_{Au} legend in (d) applies to (e) also.

Next we show the effect of the incident angle and the polarization of incident light on the simulated absorber structure considering $H_{Au} = 15$ nm and $H_{sp} = 22$ nm. Figure 2(a) and 2(b), respectively, show the absorption spectrum at different incident angles and the angular variation of resonance wavelength/peak absorbance, for both the TE and TM polarizations. It can be seen that, with increasing angle of incidence, little red (blue) shift in the resonance wavelength is observed for TE (TM) polarized incident light and the absorbance remains unchanged up to 40° deviation from the normal for both the TE and TM case. A rapid decrease in peak absorbance can be noticed for TE (TM) polarizations beyond the incident angle 60° (70°). Furthermore, within a bandwidth of 10 nm around perfect absorption wavelength and angular width of 60° , more than 90 % absorbance is achieved for both polarizations.

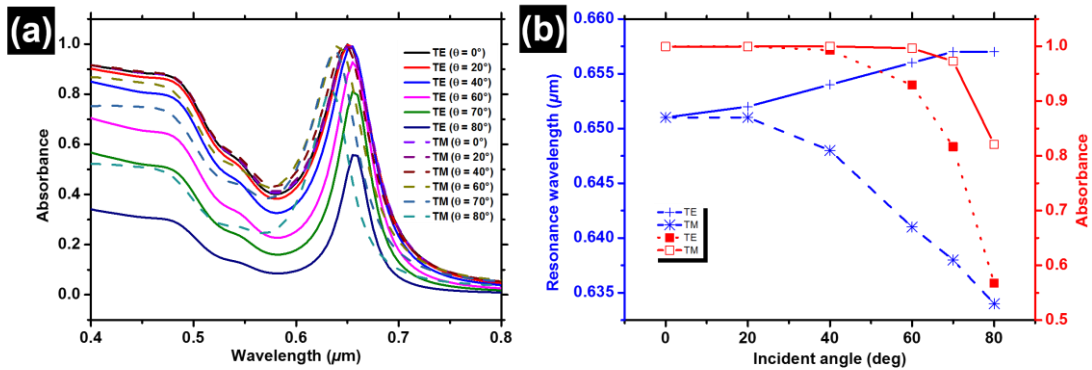


Figure 2. (a) Absorption spectra at different incident angles and (b) the angular variation of resonance wavelength/peak absorbance, for both the TE and TM polarizations.

3.2. Absorber fabrication via block copolymer engineered metasurfaces. Guided by simulations as discussed in Figure 1 for the optimal gap plasmon absorber system, we employed a cylinder forming PS-*b*-PMMA BCP (total $M_n = 205$ kg mol^{-1}) to produce a hexagonally ordered template with pitch of ca. 69 nm (d_{c-c}) and diameter of 42 nm. The process steps used are shown in Figure 3 below. Optimized pattern formation of the high

molecular weight PS-*b*-PMMA self-assembly was achieved through the blending of a low molecular weight (total $M_n = 10 \text{ kg mol}^{-1}$) lamellar PS-*b*-PMMA acting as a plasticizer, as reported previously (see Figure 3b).[39],[44] SI Figure S2a-c displays poorly organized PS-*b*-PMMA features on Al_2O_3 surfaces directly after spin casting. Well-ordered PS-*b*-PMMA features were then achieved after annealing at 230°C for 90 mins as shown in SI Figure S2d-f. PS-*b*-PMMA BCP templates were subsequently rendered porous following selective PMMA block etching through UV exposure, acetic acid immersion, and reactive ion plasma etching (see Figure 3c).

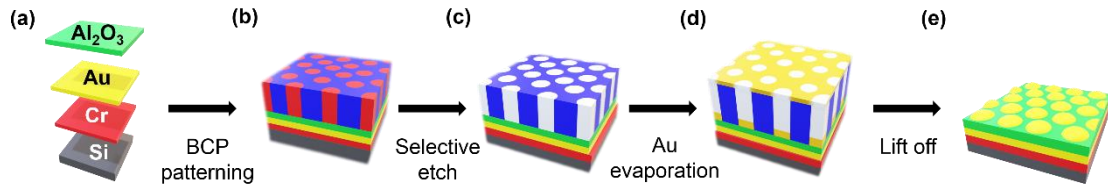


Figure 3. Process steps for the fabrication of an ultrathin Au gap plasmon absorber system.

Figure 4a displays a top-down SEM image of the porous PS template after self-assembly and PMMA removal. (See the experimental section for a detailed description). Figure 4(b) and 3(c) display the corresponding GISAXS 2D pattern and $I(q_y)$ spectrum exhibiting up to five structure factor peaks inferring the long-range order of the hexagonal pattern and the vertical nature of the pores. The center-to-center cylinder inter distance (d_{c-c}) of 69 nm and diameter (D) of 42 nm were calculated from the SEM and GISAXS study. Next, Au deposition and lift-off process was carried out using the porous PS template to fabricate Au nanoresonators as shown in Figure 3(d) and Figure 4(d). The GISAXS $I(q_y)$ spectrum after Au deposition and polymer removal is shown in Figure 3f and differs from that of the hole array. Indeed, the Au nanoresonator form factor is significantly enhanced owing to the strong electron density contrast of Au in comparison to the original polymer

template. This form factor modulation is also clear on the 2D GISAXS pattern (Figure 4e). Nevertheless, the first structure peak is only moderately shifted and the characteristic sizes of the Au metasurfaces match accordingly with the original PS template, *i.e.* $d_{c-c} = 68$ nm and $D = 42$ nm.

Corroborating evidence that aided in optimizing the patterning process was assessed by X-ray reflectivity and are detailed in SI Figure S4. Figure 4g shows a STEM image detailing the cross-sectional profile of the fabricated Au MS structure. The precise imaging techniques shows that the Au nanoresonators derived from the BCP template have a reproducible shape with circular symmetry from the top view (Figure 4d) and rounded edges from the side view (Figure 4g). We also observe clearly the uniform nature of the deposited Al₂O₃ spacer and Au reflector layers.

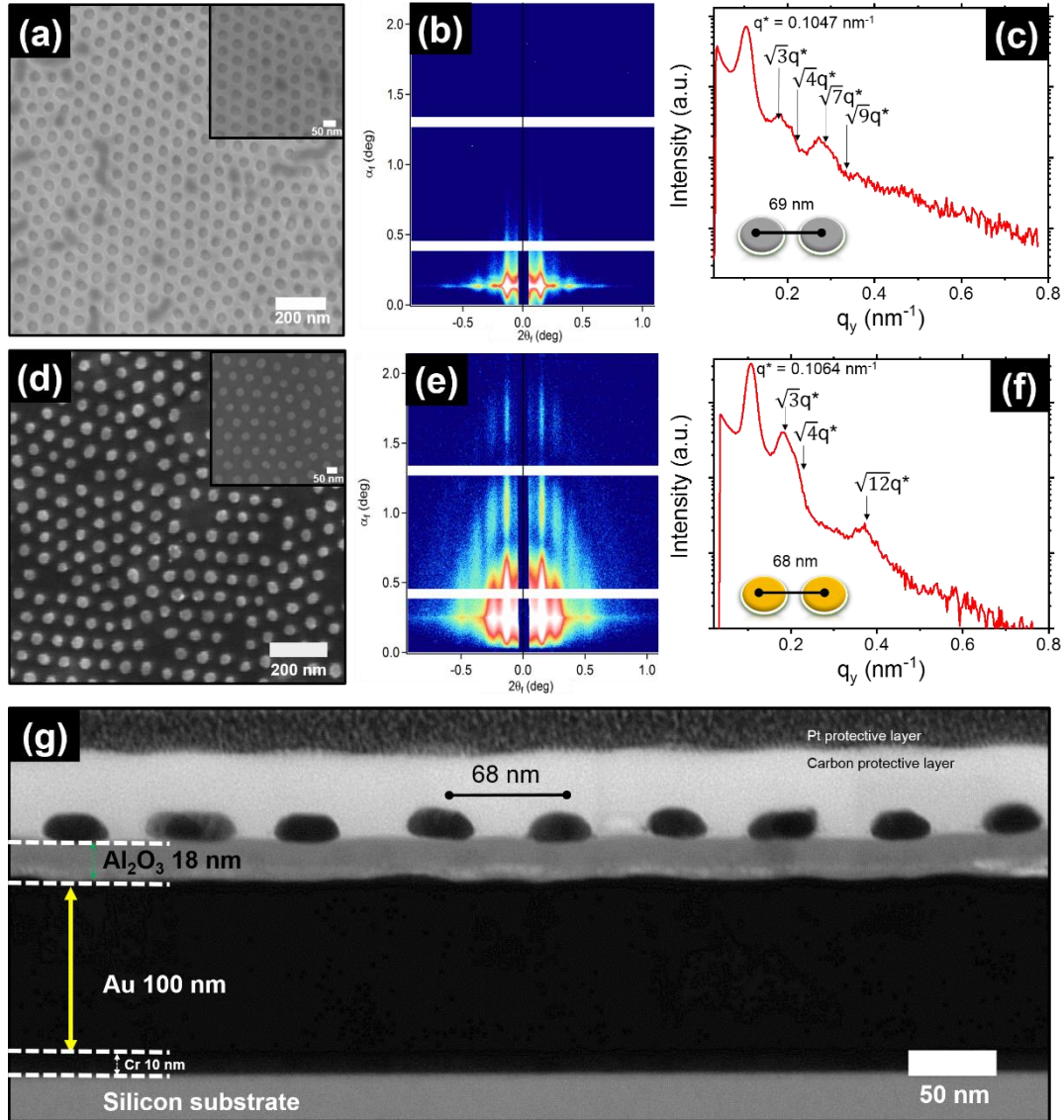


Figure 4. (a) Top-down SEM image of porous PS template after PMMA etch removal from PS-*b*-PMMA BCP cylindrical template. (b) GISAXS 2D scattering pattern of the PS template. (c) Corresponding $I(q_y)$ spectrum of the PS template. (d) Top-down SEM image of the Au nanoresonators (15 nm height) formed after lift-off process using the template shown in (a). (e) GISAXS 2D scattering pattern of the Au metasurface. (f) Corresponding $I(q_y)$ spectrum of the Au metasurface. (g) STEM image of the Au metasurface revealing the cross-sectional profile of the fabricated bilayer absorber comprised of a Au reflector layer (100 nm), Al_2O_3 spacer layer (18 nm after 200 ALD cycles) and the rounded Au MS = 68 nm (d_{c-c}), $D = 42$ nm, and Au height, $H_{\text{Au}} = 15$ nm.

3.3. Optical properties. Figure 5 shows that the absorption response of the fabricated Au gap plasmon absorber is significantly influenced by the Au resonator height and Al₂O₃ spacer layer thickness. Firstly, Figure 5(a) shows that only 20% absorption at 660 nm resulted from Au MS arrays possessing 5 nm height on an Al₂O₃ spacer thickness of 9 nm (black line). Interestingly, we see that by increasing the Al₂O₃ spacer thickness, *e.g.* 27 nm (green line), 47% absorption was measured for the 5 nm Au nanoresonator height, while there was no discernible shift in the absorption wavelength band. A similar trend of increased absorption with respect to a thicker Al₂O₃ spacer is also evident after transitioning to Au nanoresonator arrays with heights of 10 nm (Figure 5(b)) and 15 nm (Figure 5(c)) respectively. Indeed, increasing the Au nanoresonator height on an Al₂O₃ spacer thickness of 27 nm resulted in 83% absorption for 10 nm Au height (at 620 nm) and 88% absorption (at 590 nm) for 15 nm Au height. One can distinctly observe this optical change by eye when inspecting the inset images in Figure 5. For example, a light green color is evident for Au height of 15 nm on 9 nm Al₂O₃ while a brown color exists after increasing the Al₂O₃ spacer thickness to 27 nm. Given the evidence observed for increasing optical absorption in the ultrathin Au layers with increased spacer layer thickness, we also analyzed the behavior of Au nanoresonators with 15 nm height atop a 42 nm Al₂O₃ spacer layer. Here, we observed a blueshift of the band wavelength from 600 nm to 560 nm with near-perfect absorption (95 %). The comparative graph in Figure 5(d) provides a complete overview of the influencing parameters, showing the maximum absorption value as a function of the Au nanoresonator heights on different Al₂O₃ spacer thicknesses.

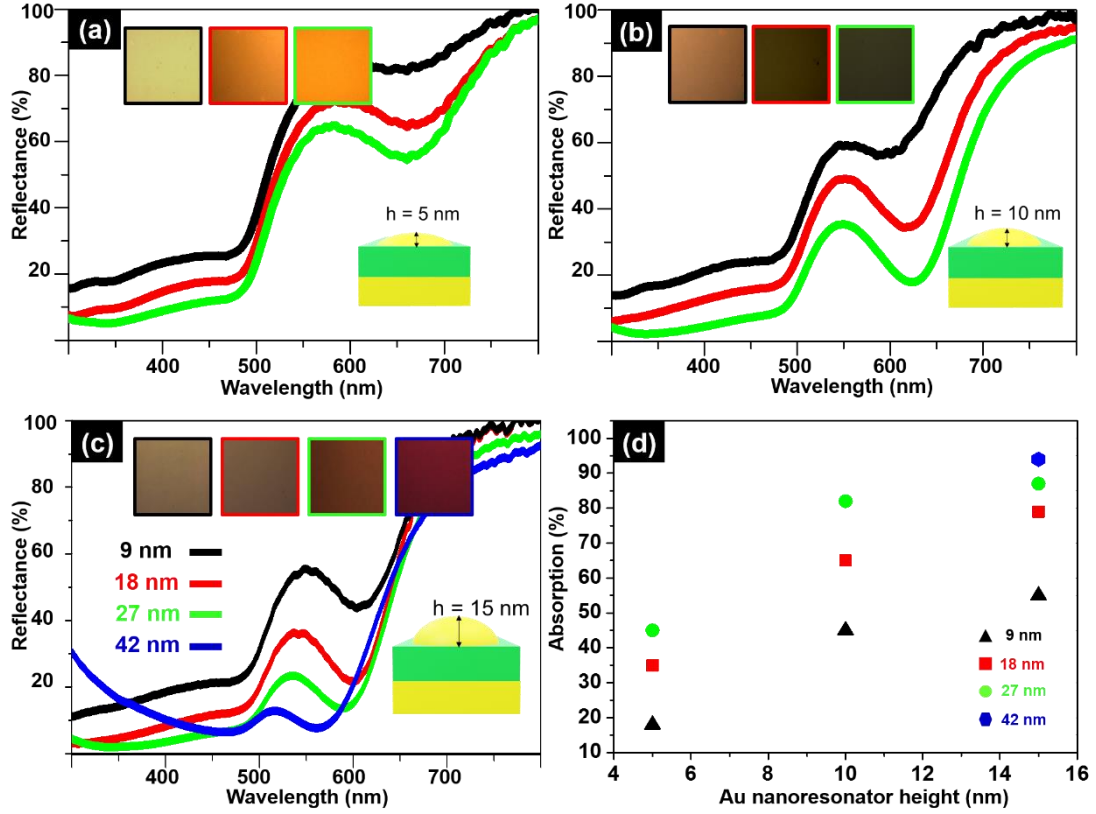


Figure 5. Relative reflectance (%) versus wavelength (nm) is shown for various Au nanoresonator heights of 5 nm (a), 10 nm (b), and 15 nm (c). Each plot shows the corresponding absorption enhancement with respect to increasing Al₂O₃ spacer thickness, *i.e.* 9 nm (black line), 18 nm (red line), 27 nm (green line) and 42 nm (blue line). Insets in each graph show optical image of respective surface (120 x 120 micron). Note that the outline color of the optical images correspond to curve color for each Al₂O₃ spacer thickness. (d) Maximum absorption on the 550-750 nm wavelength range as a function of the Au nanoresonator height (5-15 nm) for different Al₂O₃ spacer layer thicknesses.

In **Figure 6**, the variation of absorbance of the fabricated structure with H_{Au} is compared with the numerically designed structures, for different values of H_{Sp} . The experimental and numerical results are only remotely similar. The fabricated structures show an absorbance less than 50 % for $H_{Au} = 5$ nm, while on the contrary, the simulated absorbance is more than 80%, for the considered values of H_{Sp} . Furthermore, the experimental absorbance is found to be increasing on the explored H_{Sp} range and seems to reach a maximum at the highest H_{Sp} values for all H_{Au} , whereas the simulated

absorbance for the initial design has comparatively less variation and reaches a maximum for moderate H_{sp} values. These differences are unlikely to be solely due to structural defects in the MS, such as polydispersity of the Au nanoresonators or non-uniform thickness of the spacer layer, since the STEM data reported above shows excellent control and homogeneity of the structural features.

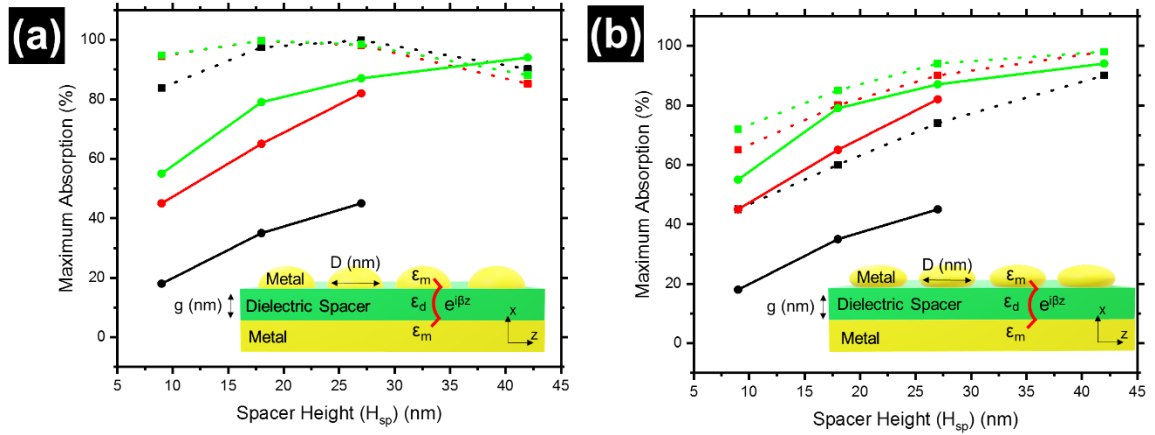


Figure 6. (a) Maximum absorption as a function of spacer thickness as obtained by experiments (continuous lines) and by initial design (dashed dots) for three different values of the Au nanoresonator height (H_{Au}): 5 nm (black), 10 nm (red), and 15 nm (green). Initial design data are a selection of that shown previously in Figure 1 for nanoresonators with spherical cap shape. Cross-section of gap plasmon absorber (inset). The lines between data points are guides for the eye. (b) Maximum absorption as a function of spacer thickness when Au nanoresonators have an oblate ellipsoidal shape. Inset shows the cross-section of the gap plasmon absorber with an oblate ellipsoidal shape.

In the gap plasmon absorber, the absorption maximum may be understood as the resonance of a Fabry-Perot-like cavity metal-insulator-metal gap plasmon mode guided between the metal film and the metal nanoparticle nanoresonator that oscillates back-and-forth between the edges of the nanoresonator. [45] If $r = |r| \exp(i\phi)$ is the reflection coefficient at the edges of the cavity of length D , and if β is the propagation constant of

the gap plasmon, the field amplitude in the cavity will be proportional to $1/(1 - |r|^2 \exp[i2(\beta D + \phi)])$, and a resonance is reached whenever

$$\text{Re}(\beta) D = m\pi - \phi \quad (1)$$

where m is an integer. Using the notation of Nielsen *et al.*, [45] we introduce the phase factor $\eta = (1 - \phi/\pi)/2$ and considering the fundamental mode ($m = 1$), we are left with the compact resonance condition as follows:

$$\text{Re}(\beta) = 2\pi \eta/D \quad (2)$$

Using an analytic approximation of the mode propagation constant for $g \ll \lambda$, [46]

$$\beta = \frac{2\varepsilon_d}{\varepsilon_m} \frac{1}{g} \quad (3)$$

where ε_d and ε_m are the dielectric constant of the dielectric gap material and the metal surrounding the gap, respectively. Combining (2) and (3), we finally find that the gap thickness g^* for which the maximum absorption resonance is reached satisfies the following relation:

$$g^* = \frac{D}{\pi} \frac{\varepsilon_d \text{Re}(\varepsilon_m)}{|\varepsilon_m|^2} \frac{1}{\eta}$$

Nielsen *et al.* [45] have shown that η decreases in case of increased leakage at the edges of the metal dot-defined cavity, while Powell *et al.* have shown that leakage is increased under metal dot antennas when the corners of the antenna are rounded.[47] Therefore, we can suggest that the resonance occurs for larger values of g^* than in the numerical design, because the rounded shapes of the Au dots lead to some leakage of the confined field, not considered in the simulations of the initial design, and consequently a decreased value of the phase parameter η . Interestingly, this leakage does not affect significantly the efficiency of the resonance since the system reaches 95% absorption. On the other hand, increasing the gap thickness g (or H_{sp} in our system) presents no technical difficulty,

whereas experimentally obtaining sharp edges in Au nanostructures can be viewed as both a challenging task as well as an opportunity for future studies. For example, wet or dry etching of Au features may be a possible route to fabricate sharp edges of BCP aligned Au nanorods[48] or particles[49] as previously reported. To explore the smooth edge hypothesis that could explain the reduced performance compared to the initial design, additional simulations were performed with oblate ellipsoidal Au nanoresonators of height (short axis) H_{Au} and diameter (long axis) D , as a way to model nano-objects with a smooth surface. The results, displayed in Figure 6 (b), show a much closer agreement with the experimental behavior. This confirms that the maximum absorption is shifted to larger values of H_{sp} when the Au nanoresonators have an oblate ellipsoidal shape and no sharp edges at the dielectric spacer surface.

4. Conclusions

Designing perfect absorbers based on thin-film processing is advantageous from a nanomanufacturing standpoint, *e.g.* spin-coating, wafer-scale patterning, and vacuum deposition of metallic films aligns well with traditional integrated circuit nanofabrication. The work demonstrated in this article shows a viable methodology toward large-scale fabrication, both in terms of processing materials and absorber performance for realizing scalable flat optics. Thin BCP templates, used here for defining Au resonators shape and in-plane organization, are at a mature stage for industry integration. Comparatively, the performance of the produced MS-based absorbers giving near-perfect visible absorption is impressive since a very low metallic content volume is required. The theoretical and experimental parameters studies presented here increase our knowledge of fabricated Au gap plasmon perfect absorber systems.

MSs present a viable means for optical component fabrication owing to their lightweight, compact and ultra-thin nature that are demanded for modern portable device requirements. In this article, we have illustrated a simple and direct approach to achieving near-perfect absorption with a large-scale MS fabrication strategy. Tunable visible light absorption bands were attained depending on Au nanoresonator heights and Al₂O₃ spacer layer (*ca.* 9-42 nm). Overall, the innate ability to dial-in perfect visible absorption from this strategy holds immense promise for photodetectors, medical diagnostics, emitters, and energy harvesting technologies.

■ AUTHOR INFORMATION

* Corresponding Authors:

C.C. - cian.a.cummins@gmail.com ORCID 0000-0001-6338-3991

G.F. - guillaume.fleury@u-bordeaux.fr ORCID 0000-0003-0779-191X

V.P. - virginie.ponsinet@crpp.cnrs.fr ORCID 0000-0002-0301-5932

Notes

The authors declare no competing financial interest.

■ ACKNOWLEDGMENTS

The authors are sincerely grateful for financial support from the University of Bordeaux and the LabEx AMADEus (ANR-10-LABEX-0042-AMADEUS) within the Bordeaux IDEX ANR-10-IDEX-003-02. This work was performed within the framework of the Equipex ELORPrintTec ANR-10-EQPX-28-01 with the help of the French state's Initiative d'Excellence Bordeaux IdEx ANR-10-IDEX-003-02. The authors also sincerely thank the LCPO support staff: Aude Manson, Melanie Bousquet, Ellena Karnezis, and Gilles Pecastaings.

REFERENCES

- [1] M.A. Kats, D. Sharma, J. Lin, P. Genevet, R. Blanchard, Z. Yang, M.M. Qazilbash, D.N. Basov, S. Ramanathan, F. Capasso, *Applied Physics Letters*, 101 (2012) 221101.
- [2] M. ElKabbash, K.V. Sreekanth, Y. Alapan, M. Kim, J. Cole, A. Fraiwan, T. Letsou, Y. Li, C. Guo, R.M. Sankaran, U.A. Gurkan, M. Hinczewski, G. Strangi, *ACS Photonics*, 6 (2019) 1889-1894.
- [3] Z. Zhang, Z. Yu, Y. Liang, T. Xu, *Opt. Mater. Express*, 8 (2018) 463-468.
- [4] J. Rensberg, Y. Zhou, S. Richter, C. Wan, S. Zhang, P. Schöppe, R. Schmidt-Grund, S. Ramanathan, F. Capasso, M.A. Kats, C. Ronning, *Physical Review Applied*, 8 (2017) 014009.
- [5] Z. Wang, Z.M. Zhang, X. Quan, P. Cheng, *Solar Energy*, 159 (2018) 329-336.
- [6] F. Monticone, A. Alù, *Reports on Progress in Physics*, 80 (2017) 036401.
- [7] D.G. Baranov, A. Krasnok, T. Shegai, A. Alù, Y. Chong, *Nature Reviews Materials*, 2 (2017) 17064.
- [8] C. Ji, K.-T. Lee, T. Xu, J. Zhou, H.J. Park, L.J. Guo, *Advanced Optical Materials*, 5 (2017) 1700368.
- [9] A. Moreau, C. Ciraci, J.J. Mock, R.T. Hill, Q. Wang, B.J. Wiley, A. Chilkoti, D.R. Smith, *Nature*, 492 (2012) 86-89.
- [10] N. Liu, M. Mesch, T. Weiss, M. Hentschel, H. Giessen, *Nano Letters*, 10 (2010) 2342-2348.
- [11] P.T. Bowen, A. Baron, D.R. Smith, *Physical Review A*, American Physical Society 2017, pp. 033822.
- [12] P.T. Bowen, A. Baron, D.R. Smith, *Physical Review A*, 93 (2016) 063849.
- [13] N. Yu, F. Capasso, *Nat Mater*, 13 (2014) 139-150.
- [14] V. Ponsinet, A. Baron, E. Pouget, Y. Okazaki, R. Oda, P. Barois, *EPL*, 119 (2017) 14004.
- [15] S. Chang, X. Guo, X. Ni, *Annual Review of Materials Research*, 48 (2018) 279-302.
- [16] R. Alaei, M. Albooyeh, C. Rockstuhl, *Journal of Physics D: Applied Physics*, 50 (2017) 503002.
- [17] R. Dezert, P. Richetti, A. Baron, *Opt. Express*, 27 (2019) 26317-26330.
- [18] G.E. Akinoglu, E.M. Akinoglu, K. Kempa, M. Giersig, *Opt. Express*, 27 (2019) 22939-22950.
- [19] K. Aydin, V.E. Ferry, R.M. Briggs, H.A. Atwater, *Nature communications*, 2 (2011) 517-517.
- [20] H.-T. Chen, *Opt. Express*, 20 (2012) 7165-7172.
- [21] A. Khan, M. Amin, *Plasmonics*, 12 (2016) 257-262.
- [22] A. Baron, A. Aradian, V. Ponsinet, P. Barois, *Comptes-Rendus-Physique*, 21 (2020) 443-465.
- [23] G.M. Akselrod, J. Huang, T.B. Hoang, P.T. Bowen, L. Su, D.R. Smith, M.H. Mikkelsen, *Advanced Materials*, 27 (2015) 8028-8034.
- [24] T. Cao, K. Liu, L. Lu, H.-C. Chui, R.E. Simpson, *ACS Applied Materials & Interfaces*, 11 (2019) 5176-5182.
- [25] H. Zhang, Y. Li, X. Long, J. Luo, Y. Zhang, M. Song, J. Fang, C. Guan, Y. Cheng, H. Liu, *Journal of Materials Chemistry C*, 8 (2020) 12876-12885.
- [26] C. Cummins, R. Lundy, J.J. Walsh, V. Ponsinet, G. Fleury, M.A. Morris, *Nano Today*, 35 (2020) 100936.
- [27] F. Ferrarese Lupi, T.J. Giammaria, A. Miti, G. Zuccheri, S. Carignano, K. Sparnacci, G. Seguíni, N. De Leo, L. Boarino, M. Perego, M. Laus, *ACS Nano*, 12 (2018) 7076-7085.
- [28] A. Alvarez-Fernandez, F. Nallet, P. Fontaine, C. Cummins, G. Hadziioannou, P. Barois, G. Fleury, V. Ponsinet, *RSC Advances*, 10 (2020) 41088-41097.
- [29] A. Alvarez-Fernandez, G. Fleury, V. Ponsinet, P.M. Walmsness, M. Kildemo, *Journal of Vacuum Science & Technology B*, 38 (2020) 013601.
- [30] N. Demazy, C. Cummins, K. Aissou, G. Fleury, *Advanced Materials Interfaces*, 7 (2020) 1901747.
- [31] M. Stefik, S. Guldin, S. Vignolini, U. Wiesner, U. Steiner, *Chemical Society Reviews*, (2015).
- [32] M.A. Morris, *Microelectronic Engineering*, 132 (2015) 207-217.
- [33] S. Ji, L. Wan, C.-C. Liu, P.F. Nealey, *Progress in Polymer Science*, 54 (2016) 76-127.
- [34] A. Alvarez-Fernandez, C. Cummins, M. Saba, U. Steiner, G. Fleury, V. Ponsinet, S. Guldin, *Advanced Optical Materials*, (2021) 2100175.

- [35] C. Cummins, T. Ghoshal, J.D. Holmes, M.A. Morris, *Advanced materials* (Deerfield Beach, Fla.), 28 (2016) 5586-5618.
- [36] H. Hulkkonen, A. Sah, T. Niemi, *ACS Applied Materials & Interfaces*, 10 (2018) 42941-42947.
- [37] C. Hägglund, G. Zeltzer, R. Ruiz, I. Thomann, H.-B.-R. Lee, M.L. Brongersma, S.F. Bent, *Nano Letters*, 13 (2013) 3352-3357.
- [38] A. Alvarez-Fernandez, K. Aissou, G. Pécastaings, G. Hadziioannou, G. Fleury, V. Ponsinet, *Nanoscale Advances*, 1 (2019) 849-857.
- [39] J.Y. Kim, H. Kim, B.H. Kim, T. Chang, J. Lim, H.M. Jin, J.H. Mun, Y.J. Choi, K. Chung, J. Shin, S. Fan, S.O. Kim, *Nature Communications*, 7 (2016) 12911.
- [40] D. Gigmes, P.-E. Dufils, D. Glé, D. Bertin, C. Lefay, Y. Guillaneuf, *Polymer Chemistry*, 2 (2011) 1624-1631.
- [41] Z. Jiang, *Journal of Applied Crystallography*, 48 (2015) 917-926.
- [42] M. Bjorck, G. Andersson, *Journal of Applied Crystallography*, 40 (2007) 1174-1178.
- [43] <https://refractiveindex.info/>, (Accessed May 2021).
- [44] D.O. Shin, J.-R. Jeong, T.H. Han, C.M. Koo, H.-J. Park, Y.T. Lim, S.O. Kim, *Journal of Materials Chemistry*, 20 (2010) 7241-7247.
- [45] M.G. Nielsen, D.K. Gramotnev, A. Pors, O. Albrektsen, S.I. Bozhevolnyi, *Opt. Express*, 19 (2011) 19310-19322.
- [46] P. Lalanne, S. Coudert, G. Duchateau, S. Dilhaire, K. Vynck, *ACS Photonics*, 6 (2019) 4-17.
- [47] A.W. Powell, D.M. Coles, R.A. Taylor, A.A.R. Watt, H.E. Assender, J.M. Smith, *Advanced Optical Materials*, 4 (2016) 634-642.
- [48] F. Lai, T. Borca-Tasciuc, J. Plawsky, *Nanotechnology*, 26 (2015) 055301.
- [49] M.S. Onses, C.-C. Liu, C.J. Thode, P.F. Nealey, *Langmuir*, 28 (2012) 7299-7307.